Additive Manufacturing Letters 1 (2021) 100022

Contents lists available at ScienceDirect

Additive Manufacturing Letters

journal homepage: www.elsevier.com/locate/addlet

Oxidation induced mechanisms during directed energy deposition additive manufactured titanium alloy builds

Caterina Iantaffi[a,b,*], Chu Lun Alex Leung[a,b], Yunhui Chen[a,b], Shaoliang Guan[c,d], Robert C. Atwood[e], Jedsada Lertthanasarn[f], Minh-Son Pham[f], Martina Meisnar[g], Thomas Rohr[h], Peter D. Lee[a,b,*]

[a] Mechanical Engineering, University College London, Torrington Place, London WC1E 7JE, United Kingdom
[b] Research Complex at Harwell, Rutherford Appleton Laboratory, Oxfordshire OX11 0FA, United Kingdom
[c] School of Chemistry, Cardiff University, Cardiff CF103AT, United Kingdom
[d] HarwellXPS, Research Complex at Harwell, Rutherford Appleton Laboratory, Oxfordshire OX11 0FA, United Kingdom
[e] Diamond Light Source Ltd, Harwell Campus, Oxfordshire OX11 0DE, United Kingdom
[f] Department of Materials, Imperial College London, London SW7 2AZ, United Kingdom
[g] ESA-RAL Advanced Manufacturing Laboratory, Harwell-Oxford Campus, Fermi Avenue, Didcot OX11 0FD, United Kingdom
[h] European Space Agency, ESTEC, Keplerlaan 1, PO Box 299, Noordwijk 2200 AG, Netherlands

ARTICLE INFO

Keywords:
Titanium alloys
Oxidation
Laser additive manufacturing
Directed-energy deposition

ABSTRACT

To prevent oxygen contamination, additive manufacturing (AM) techniques normally operate in an inert gas chamber (GC). An alternative method, useful for large builds and components repair, is the application of localised shielding gas (LSG). The effect of oxygen contamination on Ti6242 during directed energy deposition (DED) AM using an inert GC compared to LSG was investigated by *in situ* synchrotron x-ray experiments. When processing in LSG mode, the amount of oxygen absorbed from the atmosphere was sufficient to reverse the Marangoni flow leading to an alteration of the molten pool geometry and strongly influencing defect formation. Microstructural analysis reveals that, at high oxygen levels, the commonly developed α' martensitic microstructure was completely suppressed, forming precipitation of a tetra modal microstructure of α phase consisting of globular, primary and secondary lamellae (in colonies) and basketweave structure. These results help elucidate the influence of oxygen contamination in additively manufactured Ti alloys, potentially enabling improved industrial practices for AM of titanium alloy.

1. Introduction

Metal additive manufacturing (AM) offers unprecedented advantages over conventional manufacturing routes, including high design flexibility, mass customisation, high material utilization efficiency, and shortened lead time from concepts to products [1–6]. Among different types of AM technologies, directed energy deposition additive manufacturing (DED-AM) has attracted significant attention from a wide range of industries, *e.g.* aerospace, automotive, and architecture, as it enables *in situ* repair applications and manufacturing of large scale near-net shape and/or functionally graded components [6–12]. The DED-AM process involves rapid heating/cooling cycles (10^3 to 10^5 K•s^{-1}), inducing a complex non-equilibrium solidification process. This rapid cooling may lead to defect formation (*e.g.* porosity and cracks), textured microstructure, solute segregation, and accumulation of residual stresses, potentially detrimental to the structural integrity of the AM parts [2,13–20]. The process-microstructure-properties-performance relationship in DED-AM remains unclear, making it difficult to optimise the process and product quality.

Titanium (Ti) alloys have a combination of high specific strength as well as excellent corrosion and fatigue resistance, and hence they are widely used in the aerospace industry [4,12]. One of the key processing challenges with AM of Ti and its alloys is the control of the oxygen level in the processing atmosphere as Ti has a high affinity to oxygen (O) [21]. At low oxygen levels, oxygen atoms go into the interstitial octahedral sites of the α phase providing solid solution strengthening [22]. At high oxygen levels, this leads to oxygen embrittlement, lowering the tensile strength, ductility, and fracture toughness of Ti alloys parts [23–26]. The susceptibility of oxygen levels in Ti alloys is very complex, depending on the alloy composition [23,27], phase fraction [22,28–30], grain size [31,32], and morphology of individual phases [25,33]. Currently, there is limited understanding of the critical O level and the underlying oxidation mechanisms during AM of Ti alloys [27,34].

* Corresponding author.
E-mail addresses: caterina.iantaffi.19@ucl.ac.uk (C. Iantaffi), peter.lee@ucl.ac.uk (P.D. Lee).

https://doi.org/10.1016/j.addlet.2021.100022
Received 15 October 2021; Received in revised form 12 November 2021; Accepted 17 November 2021

To prevent oxidation of Ti and its alloys, they can be processed in a vacuum or inert gas chamber (GC) [21]; however, it is costly and impractical to process large near-net shaped components and to perform *in situ* repair due to the usage of a high volume of cover/shielding gas [9,24]. Prior work used a localised inert shielding gas (LSG) in DED to prevent oxidation of Ti [9,24,35], otherwise, both liquid and solid surface oxidation can simultaneously occur [21]. Liquid oxidation occurs when the molten metal remains temporarily exposed to an oxidising atmosphere [21,27]. When Ti alloys are exposed at a temperature above 440 °C and below its melting temperature, this may lead to the formation of an oxide scale (OS) [21,36]. Caballero et al. observed that the oxide scale can dissolve in successive build layer(s) during wire DED, forming an oxygen diffusion zone (ODZ) [35]. However, there is no study on the impact of oxidation in powder-based DED-AM for near α Ti alloys. A deeper understanding of oxidation mechanisms in Ti alloys under LSG conditions is essential for the qualification of industrial DED-AM technologies. Here, a DED process replicator [18] was used to enable *in situ* synchrotron x-ray imaging of the melt pool dynamics during DED-AM of Ti-6Al-2Sn-4Zr-2Mo-Si (Ti6242) under LSG and atmospheric conditions. No studies have investigated oxidation mechanisms for Ti6242 alloys [37]. Ti6242 is a near α-Ti alloy used for aerospace applications as it provides 10% higher mechanical properties and greater creep resistance than Ti-6Al-4V [37–39]. X-ray micro computed tomography (μCT), metallography, and x-ray photoelectron spectroscopy (XPS) were used to further understand the oxygen effects on defect population, microstructure evolution, and to reveal different types of oxygen species in Ti6242, respectively. The new insights explain the oxidation mechanisms for Ti6242 are dominated by liquid phase oxidation. Increasing oxygen concentration alters the melt flow behaviour and promotes crack formation and increases the $\alpha \rightarrow \beta$ transition temperature. This leads to the formation of a mixed microstructure of globular α and lamellae α' and α" and basketweave α pattern in DED-AM Ti6242. This work addresses that a good control of oxygen level can potentially be used as a processing strategy route to reduce the porosity and tailor microstructure in DED-AM components.

2. Methods

2.1. Materials

The feedstock material used for the DED-AM process was a gas atomised (GA) Ti6242 powder (Goodfellow, UK). The elemental chemical composition is reported in **Supplementary Table 1**. The powder morphology was examined by scanning electron microscopy (SEM) in the secondary electron imaging mode at 20 kV (JEOL JSM-6610LV, Tokyo). The powder particles are spherical in shape, with few satellite particles. The cumulative particles size distribution and median (D_{50}) is 59.5 μm (see details in **Supplementary Figure 1**).

2.2. DED and in situ synchrotron x-ray radiography

Here, a Blown Powder Additive Manufacturing Process Replicator (BAMPR) replicates an industrial DED-AM machine (see details in ref [18] and in **Supplementary Methods**). The DED-AM takes place in a gas chamber where an inert gas is purged and maintained within it to keep the oxygen level below 5 ppm. In the LSG condition, the chamber was left open and only the shielding argon gas was used during DED-AM. Processing parameters are reported in **Supplementary Table 2**. BAMPR was integrated onto the beamline I12 Joint Engineering, Environmental, and Processing (JEEP), at the Diamond Light Source (DLS, UK). This enabled *in situ* visualisation of the laser-matter interactions during DED and interpretation of molten pool features, including pore migration and molten pool morphology.

2.3. Sampling and ex situ analysis

The DED samples from the *in situ* x-ray imaging experiments were examined by micro-computed tomography (μCT) using a NikonXTH225 (Nikon, Japan) to image and quantify internal defects. The data were reconstructed using the embedded algorithms in CT Pro (Nikon), resulting in a voxel size of 7.8 × 7.8 × 7.8 μm [3]. The image analysis was performed using Avizo 9.3 (ThermoFisher) [40]. Metallurgical analysis has been carried out on sectioned samples using a scanning electron microscope (SEM) and electron back-scattered diffraction (EBSD). SEM micrographs were captured by secondary electron imaging using a Zeiss Gemini Sigma300 FEG SEM system with an accelerating voltage between 5 and 10 keV and a 30 μm aperture. EBSD maps were captured on the same microscope equipped with a Bruker Argus high-definition electron backscatter detector using 0.4 μm pixel size, 20 keV accelerating voltage, and 120 μm aperture size.

3. Results and discussion

Selected radiographs from the gas chamber (GC) and localised inert shielding gas (LSG) conditions are shown in **Fig. 1**. Distinctive melt pool behaviours are observed including Marangoni flow, pores behaviour and melt pool morphology. The time resolved radiographs, reveal the pores positions and movements which indicate the molten metal flow directions. The pores are observed to follow an outward pattern in the GC condition which indicates the centrifugal Marangoni flow direction in the time series radiographs, see **Fig. 1b-d** and **Supplementary Video 1**. In contrast, an inward centripetal Marangoni flow is observed in the LSG condition, see **Fig. 1g-i** and **Supplementary Video 2**. Lee et al. [41] and Mills et al. [42] showed that the direction of the molten metal flow is determined by surfactants contents such as sulfur or oxygen. The molten metal flow is dominated by the Marangoni forces, which in turn are driven by the surface tension gradient ($\frac{d\gamma}{dT}$) [42,43]. The molten metal fluid moves from an area with low surface tension to an area with high surface tension to minimise free energy. When the surface tension gradient is negative (**Fig. 1e**), the melt flow is radially outward, carrying the hot metal to the edges of the melt pool. In general, it is assumed that the Marangoni forces are induced by a negative surface tension gradient and thus, the Marangoni flow is an outward flow of the molten metal. The flow direction reverses when the temperature coefficient of surface tension reverses. The absence of protective Ar gas in the LSG condition means there is a higher oxygen partial pressure above the molten pool, with more oxide forming, and being swept into the pool and distributed into the bulk track of Ti6242 formed. The dissolved oxygen species act as surfactants [43–47], altering the temperature coefficient of the molten alloy's surface tension from negative to positive, reversing the Marangoni flow. This causes the molten metal to flow outward from the edges to the centre of the molten pool in the LSG condition, resulting in a deeper, convex molten pool shape (**Fig. 1f**). Similar phenomena have also been observed in welding and laser powder bed fusion (LPBF) [16,17]. Conversely, under inert gas chamber conditions the molten pool is shallow and concave (**Fig. 1a**). Here, we observe powder sintering during DED-AM [48] (**Fig. 1a**) and this phenomenon is absent in the LSG condition (**Fig. 1f**). Under the LSG condition, DED-AM is a more stable process as shown by the consistent melt pool shape during 5 layers build. The DED-AM part also has fewer lack of fusion defects in successive layers (see details in **Supplementary Figure 3** and **Figure 4**. We hypothesise that oxygen species in the LSG condition enhances the thermal conductivity and the laser absorption efficiency [18]. It is believed that the oxide film, formed due to the temporary exposure of the molten pool to the atmosphere in the LSG condition, works as an absorptive thin coating enhancing laser absoptivity [49,50]. In the LSG sample, the laser absorptivity is also influenced by the printed layer surface condition as oxidation may influence surface topography at the submicrometre scale [49]. The convex LSG melt pool top surface (**Fig. 1f**) illustrates good wetting of the liquid metal on the solid underlying DED

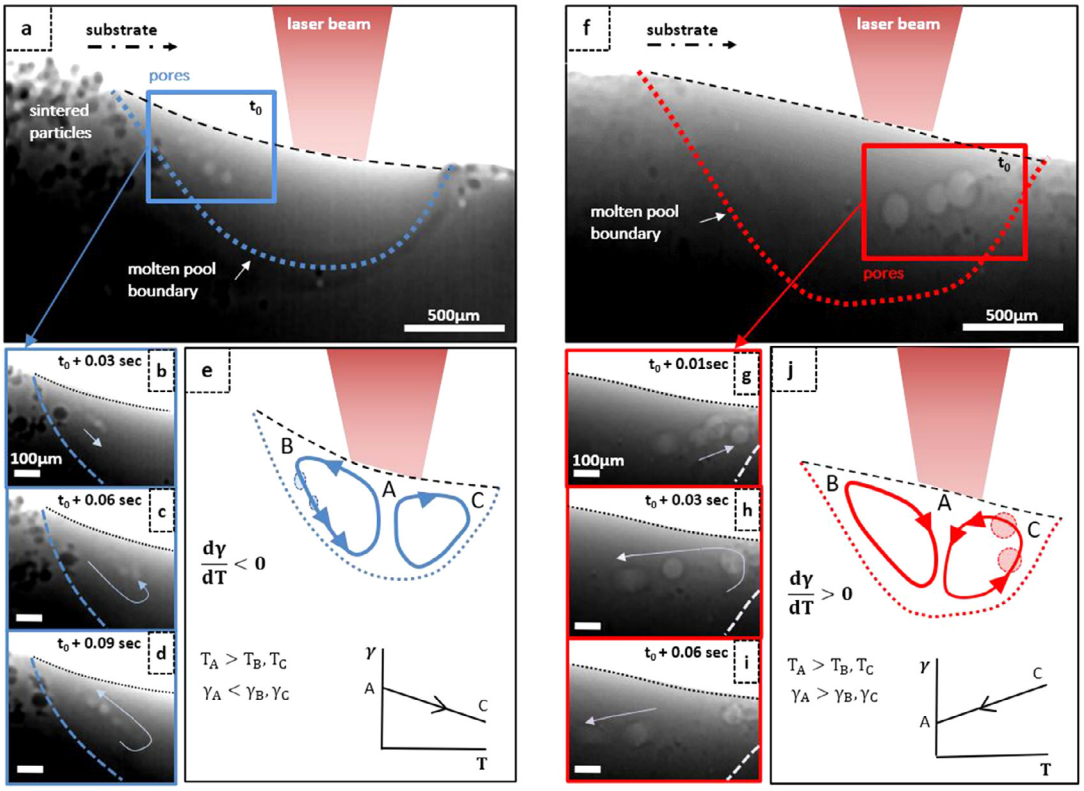

Fig. 1. Molten pool dynamics and morphology of the first layer build during DED-AM under GC a) and LSG f) conditions. Time-resolved radiographs showing pore behaviour in the b)-d) GC and g)-i) LSG conditions. e) Schematic diagram [43] for GC condition describes the molten metal flow pattern as a function of surface tension (γ) and temperature (T) in negative surface tension gradient. j) Schematic diagram for LSG describes the molten metal flow pattern as a function of γ and temperature T in positive surface tension gradient.

track. This result was unexpected, as prior studies [33,51] show the wettability of liquid metals is better on clean alloy surfaces than on oxidised ones. In a section below, we further investigate the surface chemistry of the DED track and the wetting mechanisms between Ti and its oxides using XPS.

Under the LSG condition, the pores in the melt pool are observed to be swept by the molten metal flow on the front of the molten pool whereas they are pushed towards the back of the melt pool in the GC condition [18]. Mills et al. [42] reported that the sweeping motion helps pores to escape from the solidification front, reducing porosity in the final part. Similar phenomena on the reversal of Marangoni flow and pore dynamics have been observed by Leung et al. using LPBF of Invar 36 oxidised powder. Oxidised Invar 36 powder and recycled oxidised Ti-6Al-4 V powder were shown to increase defects during AM [16,52–54]. In contrast, this study shows that the oxygen species in the molten Ti6242 produces less porosity. The reversed Marangoni flow migrates pores to the melt surface, escaping the weldpool [55], see **Supplementary Video 2.** These observations suggest that oxygen uptake of the bulk metal primarily occurs in the liquid pool rather than oxidation of the solid surface, supported by the lack of oxide scale on the final build surface (**Supplementary Figure 4**) and the good wettability of the liquid metal (**Fig. 1f**), both suggesting oxygen pickup on the solid surface is minor.

To further understand the influence of GC and LSG conditions on the build quality of the samples, μCT scans provide a 3D evaluation of internal defects distribution. The GC sample (**Fig. 2a**) contains a large number of spherical pores with a total pore volume (PV) of 0.011 mm^3. These pores have a mean sphericity (ψ) value of 0.98 and a mean equivalent diameter (D_{eq}) of 38 μm with 18 μm in standard deviation (**Fig. 2b**), see **Supplementary Methods** for equations used. Lack-of-fusion defects are observed between build layers, as similarly reported by Kobryn et al. [56], and sintered particles are observed on the surface of the GC sample. In contrast, no lack of fusion defects are detected in the LSG sample (**Fig. 2c**). The reduction of lack of fusion defects could be due to the combination of reversed Marangoni flow, less powder sintering, good wettability, and enhanced laser absorptivity. This observation conforms with **Fig. 1b**, suggesting that the change in flow direction improves the build quality, including the reduction of porosity [42] **Fig. 2c** reports the LSG sample and the enlarged view of the LSG sample in **Fig. 2d** shows a 1.4 mm crack and crack induced porosities with a PV of 0.025 mm^3 surrounding the crack and at the edge of the sample.

Bin et al. [22,57] reported that a small concentration of oxygen (up to 34 at.%) as an interstitial element can enhance the mechanical properties of α-Ti. However, our results show that high oxygen concentration causes crack propagations from the oxide scale into the bulk of the Ti6242 along α phase boundaries (see details in **Supplementary Figure 5e** and **Figure 7**. Cracks initiate at the α/β boundaries where the strain incompatibility between α and β phases is high [58]. The dissolution of oxygen occupies in the interstitial of the hexagonal close-packed (hcp) crystal lattices (α phase) causes the embrittlement of Ti6242[25,31].

Because of the significant difference of O solubility in α-Ti (14.2 wt% at 600 °C) and β-Ti (2.7 wt% at 1720 °C), α-Ti alloys are more sensitive to oxygen compared to Ti-β alloys [23]. Along with the Ti-alloy composition, the microstructure also affects Ti-alloy susceptibility to O[23]. From the literature, Ti-6Al-4 V, an α+β Ti alloy, consisting of martensite (α') reduces its ductility if the oxygen content reaches beyond 0.15 wt.% whereas a microstructure consisting of α and β phases can tolerate a critical oxygen level up to 0.36 wt.% [23]. The advantage of α/β phases mixture over the α' in tolerating much higher O content is due to the higher ratio of α to transformed β volume fraction [28]. Also, α phases morphology affects the ductility; it has been reported that crack growth and deflection is influenced by α lath morphology and texture. Tan et al.

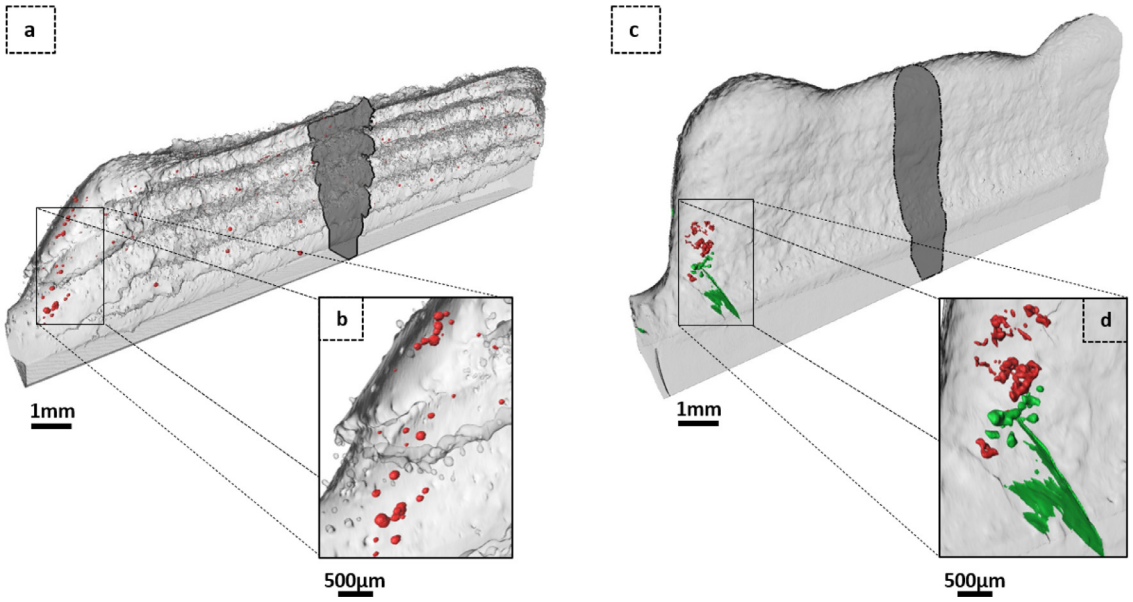

Fig. 2. µCT reconstruction of samples build by DED-AM. Pores are marked in red and cracks in green, respectively. a) GC sample and b) the enlarged view of a). b) LSG sample and d) the enlarged view of b).

66 investigated the role of microstructure in Ti alloys to tailor plastic deformation and crack growth, revealing that a combination of large globular and lamellar α phase is a good combination for a superior fracture toughness performance.

SEM and EBSD analysis were carried out on the GC and LSG samples to understand the influence of oxygen on the resultant microstructure, see **Fig. 3**. **Fig. 3a** reveals the typical ultra-fine acicular α' martensite lath structure in the GC sample [1,59–62]. **Fig. 3b** shows a tetra modal microstructure of globular α, primary and secondary lamellar α (in colonies), and basketweave structure in the LSG sample [63]. **Fig. 3c** reports the EBSD inverse pole figure build direction (IPF-BD) map of **Fig. 3a**, showing fine basketweave intertwined morphologies of α' laths. No apparent preferred texture in both the GC and LSG conditions at the observed magnifications. **Fig. 3d** illustrates the IPF-BD map of the LSG condition, showing large lamellar α. Grains in the GC condition were smaller than in the LSG condition with an average grain size of 3.01±4.41 µm and 7.19±10.11 µm under GC and LSG conditions, respectively. These differences are attributed to the presence of oxygen as a solute in the alloy. From the energy dispersive x-ray (EDX) analysis, 5 wt.% of O has been quantified in the bulk of the LSG sample, see **Supplementary Figure 6**. Atmospheric contamination and oxidation raises the α to β transus temperature (T_β) promoting the precipitation of α from β[23]. Oxygen acting as an alpha stabilizer, raises the β transus temperature ($T_\beta = 993°C$) [25,64]. This changes the equilibrium phase diagram of Ti-6242 and the α/β phases partitioning, see **Fig. 3e**. Based on the oxygen concentration, we estimate the β transus temperature has increased up to $T_\beta{}' = 1215\ °C$, using the Eq. reported by Kahveci and Welsh[29]:

$$T'_\beta = 993\ °C + 243\ °C * O_{wt\%} \quad (1)$$

With the increase of T_β, the solid-state transformation mechanism changes in LSG. The microstructure of the LSG sample exhibits tetra modal α phase rather than acicular martensite (**Fig. 3a**), this confirms that the solid-state transformation of the LSG sample begins at the α±β region instead of the β region in the GC sample, see schematic in **Fig. 3e**. A variety of microstructures showing better mechanical performance with respect to the α' martensitic structure can be obtained with appropriate post heat treatment [61,65]. Although, the intrinsic high cooling rate and high thermal gradient in AM techniques make the solidification conditions very hard to control. Tan et al. [66] recently reported a trimodal microstructure (TM) in a forged and heat treated Ti-6Al-2Sn-2Zr-3Mo-1Cr-2Nb-0.1Si alloy. The TM consists of a mixture of primary globular (α_g), lamellar α phases (α_l) and α secondary (α_s) transformed within the β matrix which has a superior fracture toughness performance [66]. Here, the DED-AM Ti-6242 with oxygen species exhibit a tetra modal α phase, see **Supplementary Figure 4c**. This microstructure deflects cracks and inhibits crack propagation as reported by references [58,66,67]. It has been reported that cracks easily propagate across equiaxed α phase but deviate when they encounter the α_l phase leading to a tortuous crack growth path [66]. Analogous resistance to crack propagation has been observed in this study, due to the diffused presence of α_l, see details in **Supplementary Figure 7**. Compared to Tan et al., we achieved the tetra modal microstructure without the need for heat treatment and may suggest a new processing strategy to engineer Ti microstructures.

Al is an α phase stabilizer and it changes the solubility of oxygen in the (α_l). Al diffuses towards the α/β interface, leading to new α' precipitations in the β phase matrix, see **Supplementary Figure 5d** This is the first time a new Al enriched β phase was observed in Ti6242, wherein the presence of oxygen has affected the elemental partitioning in the α_l lamellae. Xu et al. [59] reported a similar segregation phenomenon in SLM Ti-6AL-4 V wherein the segregation of V, a β stabiliser, promotes the formation of β phase in $\alpha + \beta$ lamellar microstructures.

Fig. 3d represents the IPF-BD map of the interlayer microstructure in the x-z plane of **Fig. 3b**, showing a banded-like structure of equiaxed α and β intergranular phases (**Supplementary Figure 8**) [68]. This is due to an increase of molten pool depth [47,69] in the LSG condition which facilitates the reheating of the previous layer between the α and $\alpha + \beta$ regions, see graphical representation in **Figure 5e**. The heat affected bands (HABs) [62] are more prominent on the two latter printed layers, suggesting that oxygen depletion continued during DED-AM, see **Supplementary Figure 5a**. Although both process parameters are the same for the GC and LSG conditions, oxygen significantly alters the phase diagram and promotes reheating of the existing microstructure towards the β phase region (GC sample) and the upper α phase region (LSG sample). This explains why we observed a homogeneous fine basketweave microstructure in the GC sample (**Fig. 3a**) and equiaxed interlayer bands in the LSG sample (**Fig. 3b**). Zhu et al. [62]. reported a similar microstructure formed due to the complex thermal history and enhanced elemental diffusivity [56]. This enhanced diffusivity boosts chemical composition

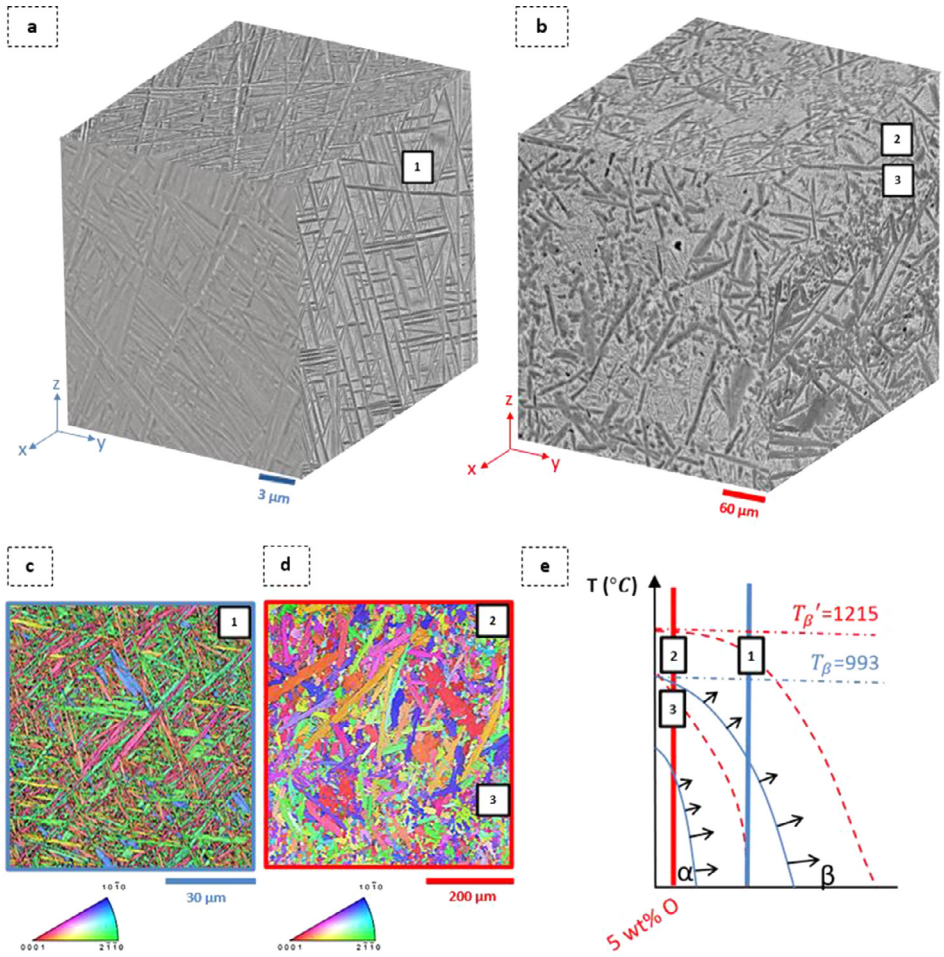

Fig. 3. Microstructural analysis of the DED samples: a) 3D SEM microstructure reconstruction of the sample manufactured in GC. b) 3D SEM microstructure reconstruction of the sample manufactured in LSG. c) shows the EBSD IPF-build direction map of a) and reveals a fine elongated needle-like α' martensitic microstructure (Widmanstätten). d) EBSD IPF-build direction map of b) showing α' lamellae with decorated globular α. e) Schematic of the temperature-oxygen content phase diagram. The diagram explains how the change in the atmosphere condition leads to a change in the observed microtexture and microstructure, in c) and d) in relation to the cooling peak temperature.

homogenization favouring α nucleating and growing from the β phase [62].

Moreover, equiaxed globular and lamellar α phases are observed just below the sample surface possibly due to the continuous oxygen depletion during DED-AM and the sample temperature remains above 400 °C [36,35]. The sample surface cools much faster than the bulk material, this induces α phase transformation from elongated lamellae to equiaxed globular α at the subsurface as shown in **Supplementary Figure 5b**.

XPS was used to further understand how oxygen species react with Ti6242 and to assess the formation mechanisms of Ti oxides. **Fig. 4a** and **4b** reveal both samples exhibit four titanium species, including: Ti $2p_{3/2}$, Ti^{2+}(TiO), Ti^{3+}(Ti_2O_3), and Ti^{4+}(TiO_2) [70]. Under the conditions studied, the LSG sample is more oxidised than the GC sample as it has 17.5% less Ti metal, Ti(0), but more Tiδ+ oxidation states. The higher oxygen concentration allows Ti to react and form $Ti^{3+}2p_{3/2}$ (Ti_2O_3), Ti^{4+}(TiO_2) and Ti^{2+}(TiO) which have a 72%, 65% and 59% increase surface area in the LSG spectra, respectively [70]. **Fig. 4c** and **4d** show that the C–O and C = O concentrations remain the same as both samples were exposed to air before XPS tests. The metal-O concentration is 15% lower in LSG due to oxidation of Ti during DED-AM. The peaks at 532.9 eV reveal the presence of silicon dioxide (SiO_2) in the LSG spectra. The presence of SiO_2 is confirmed by the peak at 103.7 eV [71] in Si2p spectra (**Fig. 4f**). Silicon (Si) is an alloying element that improve oxidation resistance in Ti alloys, refining and compacting the TiO_2 scale, promoting the diffusion of Al in the oxide scale and inhibiting the formation of rutile TiO_2 [72]. We hypothesised that here the presence of SiO_2 restrain the formation of rutile TiO_2 [73] as confirmed by oxidised species in the Ti 2p spectra (**Fig. 4a** and **4b**). As oxygen reacts with silicon to form SiO_2 rather than with Ti to form rutile, it is hypothesised that this enhances the oxidation resistance reducing the depth of oxygen diffusion. However, the difference in coefficient of thermal expansion between Ti oxides and SiO_2 can induce localised stress and promote cracks at the sample surface, as shown in **Fig. 2c** and **Supplementary Figure 5e** [74]. Similarly to Si effects, also Zirconium (Zi) is another element that can change the characteristics of the oxide scale improving Ti6242 oxidation resistance [72]. High-resolution spectra for Al, Zr and Sn reveal the presence of additional oxides species in the LSG sample, such as Al_2O_3, SnO_2 and ZrO_2 (see **Supplementary Figure 10b, 10d** and **10f**).

Conclusions

Our results elucidate the oxidation mechanisms during DED-AM in an inert gas chamber (GC) and localised shielding gas (LSG). A significant increase in oxygen level in the LSG condition was observed, with the key mechanism hypothesised to be increased oxygen uptake in the liquid pool rather than oxidation of the solid surface.

In situ x-ray imaging reveals that oxygen uptake in the liquid occurred in the LSG condition. Oxygen acts as a surface-active element, reversing the surface tension gradient and hence, the Marangoni flow, altering both the molten pool morphology and porosity formation. Under the LSG condition, the molten pool is deeper and more convex shape, sintering phenomena are suppressed. Further, the reversed Marangoni flow sweeps pores towards the surface where they are more likely to escape, resulting in a lower percentage porosity (as validated by microtomogarphy). The importance of oxygen pickup by the liquid pool, rather than through solid surface oxidation is supported by the observations that the solid has no obvious oxide scale (**Supplementary Figure 5**) and that the liquid metal wets the previously deposited layer well (**Fig. 1f**).

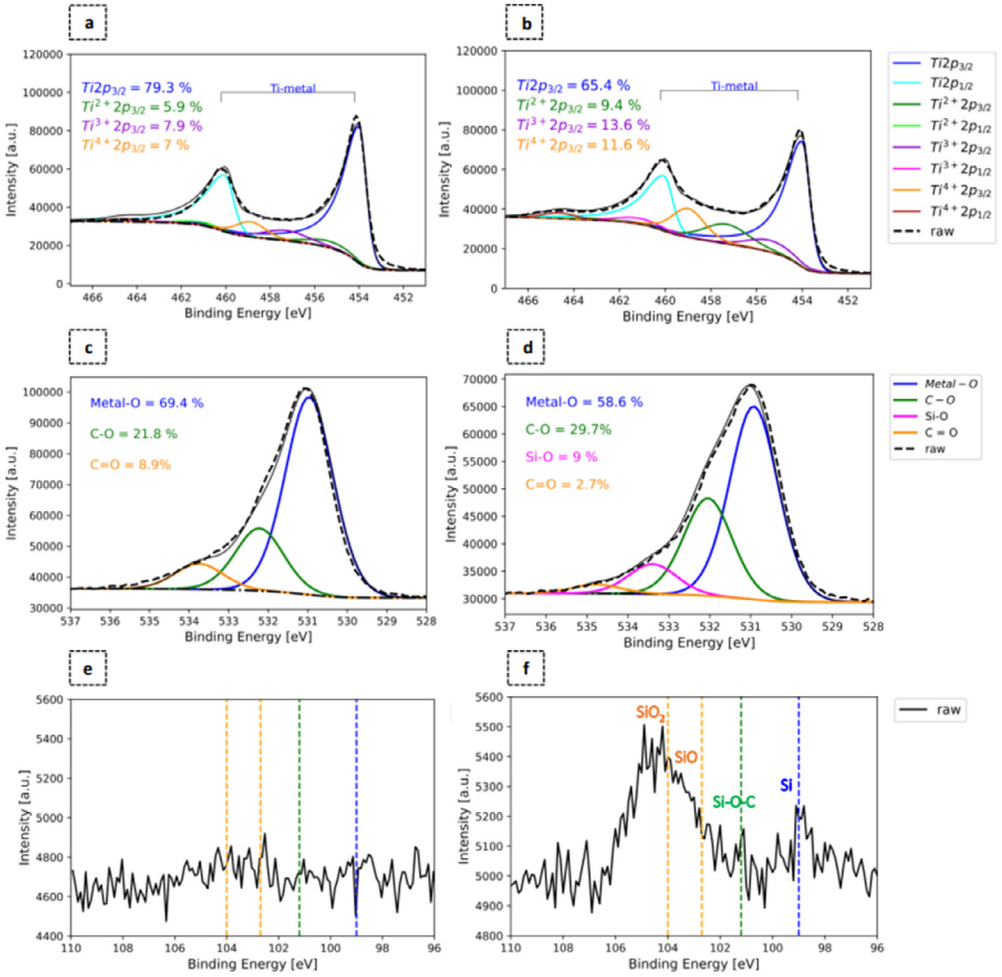

Fig. 4. XPS high resolution spectra of the main components. a) high-resolution spectra of Ti2p from the sample GC manufactured. b) high-resolution spectra of Ti2p from the sample manufactured with LSG. In the graphs on the left are reported the different Ti oxidation states concentrations. c) high resolution spectra for O1s on GC manufactured sample. d) high resolution spectra for O1s on LSG manufactured sample. e) high resolution spectra for Si2p on GC manufactured sample. f) high resolution spectra for Si2p on LSG manufactured sample with highlighted four peak regions: 99 eV Si, 101.2 eV Si-O-C, 102.7 eV SiO, 103.7 eV SiO_2. .

The microstructure analysis confirms the significant increase in bulk oxygen content in the alloy when built in the LSG condition, hypothesised to occur primarily via oxidation of the molten pool, followed by subsequent mixing into the bulk. These results in an O-enriched Ti6242 banded tetramodal microstructure. Oxygen raises the T_β, changing the solid-state transformation mechanism in LSG and inhibiting the formation of α' martensitic structure, in favour an α/β microstructure that improves the oxygen tolerance level. This encourages use of the DED process under normal atmospheric conditions.

The formation of Si and Zr oxides affects the oxide scale characteristics improving the oxidation resistance. This makes the Ti6242 alloy more resistant to oxygen diffusion than the widely used Ti-6Al-4 V.

Our insights into the oxidation phenomena during DED-AM of Ti6242 can help improve the manufacturing process stability, controlling the resultant microstructure (and defects) during DED-AM under localised shielding gas conditions.

Author contributions

PDL conceived the project. YC and CLAL designed the experiments. CI, PDL, YC, CLAL performed the beamtime. CI performed data analysis, and results interpretation with CLAL, YC, PDL, and MM contributions and guidelines. SG performed XPS analysis. JL performed EBSD analysis. CI, CLAL, and PDL led the paper writing, with all authors contributing.

Declaration of Competing Interests

The authors declare that they have no known competing financial interests or personal relationships that could have appeared to influence the work reported in this paper.

Acknowledgements

This research was supported by the European Space Agency (ESA) (through contract 4000132547 as part of ESA's Discovery Program) and MAPP: Future Manufacturing Hub in Manufacture using Advanced Powder Processes (EP/P006566/1), the Engineering and Physical Sciences Research Council (EPSRC), Royal Academy of Engineering Chair in Emerging Technology (CiET1819/10), and Rolls-Royce plc. via the Horizon 2020 Clean Sky 2 WP5.8.1 programme. CLAL is grateful for the support from the EPSRC Impact Acceleration Account (EP/R511638/1). Laboratory space and facilities were provided by the Research Complex at Harwell and the ESA–Rutherford Appleton Laboratory Advanced Manufacturing Laboratory at ESA's Harwell facility. The authors thank Diamond Light Source for providing beamtime (MT20096) and the staff at I12 beamline for technical assistance.

Supplementary materials

Supplementary material associated with this article can be found, in the online version, at doi:10.1016/j.addlet.2021.100022.

References

[1] M. Neikter, P. Åkerfeldt, R. Pederson, M.L. Antti, V. Sandell, Microstructural characterization and comparison of Ti-6Al-4V manufactured with different additive manufacturing processes, Mater. Charact. 143 (2018) 68–75.
[2] S. Gorsse, C. Hutchinson, M. Gouné, R. Banerjee, Additive manufacturing of metals: a brief review of the characteristic microstructures and properties of steels, Ti-6Al-4V and high-entropy alloys, Sci. Technol. Adv. Mater. 18 (2017) 584–610.
[3] W.E. Frazier, Metal additive manufacturing: a review, J. Mater. Eng. Perform. 23 (2014) 1917–1928.

[4] T. Wang, Y.Y. Zhu, S.Q. Zhang, H.B. Tang, H.M Wang, Grain morphology evolution behaviour of titanium alloy components during laser melting deposition additive manufacturing, J. Alloys Compd. 632 (2015) 505–513.

[5] B. Dutta, F.H Froes, (Sam. The Additive Manufacturing (AM) of titanium alloys, Met. Powder Rep. 72 (2017) 96–106.

[6] Z. Liu, B. He, T. Lyu, Y. Zou, A review on additive manufacturing of titanium alloys for aerospace applications: directed energy deposition and beyond Ti-6Al-4V, Jom 73 (2021) 1804–1818.

[7] W.J. Oh, W.J. Lee, M.S. Kim, J.B. Jeon, D.S. Shim, Repairing additive-manufactured 316L stainless steel using direct energy deposition, Opt. Laser Technol. 117 (2019) 6–17.

[8] J.H. Yu, Y.S. Choi, D.S. Shim, S.H. Park, Repairing casting part using laser assisted additive metal-layer deposition and its mechanical properties, Opt. Laser Technol. 106 (2018) 87–93.

[9] A. Saboori, et al., Application of directed energy deposition-based additive manufacturing in repair, Appl. Sci. 9 (2019).

[10] E. Uhlmann, R. Kersting, T.B. Klein, M.F. Cruz, A.V. Borille, Additive manufacturing of titanium alloy for aircraft components, Procedia CIRP 35 (2015) 55–60.

[11] M. Seifi, et al., Progress towards metal additive manufacturing standardization to support qualification and certification, Jom 69 (2017) 439–455.

[12] R. Liu, Z. Wang, T. Sparks, F. Liou, J. Newkirk, Aerospace applications of laser additive manufacturing, Laser Additive Manufacturing: Materials, Design, Technologies, and Applications, Elsevier Ltd, 2017, doi:10.1016/B978-0-08-100433-3.00013-0.

[13] M.M. Kirka, P. Nandwana, Y. Lee, R.R Dehoff, Solidification and solid-state transformation sciences in metals additive manufacturing, Scr. Mater. 135 (2017) 130–134.

[14] D. Zhang, et al., Additive manufacturing of ultrafine-grained high-strength titanium alloys, Nature 576 (2019) 91–95.

[15] Dass, A. & Moridi, A. State of the art in directed energy deposition : from additive manufacturing to materials design. 1–26 (2019) doi:10.3390/coatings9070418.

[16] C.L.A. Leung, et al., The effect of powder oxidation on defect formation in laser additive manufacturing, Acta Mater. 166 (2019) 294–305.

[17] C.L.A. Leung, et al., In situ X-ray imaging of defect and molten pool dynamics in laser additive manufacturing, Nat. Commun. 9 (2018) 1–9.

[18] Chen, Y. et al. In situ and Operando X-ray imaging of directed energy deposition additive manufacturing. 1–31 (2020).

[19] P.C. Collins, D.A. Brice, P. Samimi, I. Ghamarian, H.L Fraser, Microstructural control of additively manufactured metallic materials, Annu. Rev. Mater. Res. 46 (2016) 63–91.

[20] C. Qiu, et al., Fabrication of large Ti-6Al-4V structures by direct laser deposition, J. Alloys Compd. 629 (2015) 351–361.

[21] M.J. Bermingham, J. Thomson-Larkins, D.H. St John, M.S. Dargusch, Sensitivity of Ti-6Al-4V components to oxidation during out of chamber wire + arc additive manufacturing, J. Mater. Process. Technol. 258 (2018) 29–37.

[22] S. Bin, L.I. Shufeng, I. Hisashi, J. Umeda, K. Katsuyoshi, Oxygen solid solution strengthened pure titanium powder materials †, Trans. JWRI 41 (2012) 59–64.

[23] M. Yan, et al., Review of effect of oxygen on room temperature ductility of titanium and titanium alloys, Powder Metall 57 (2014) 251–257.

[24] A. Carrozza, et al., An innovative approach on directed energy deposition optimization: a study of the process environment's influence on the quality of Ti-6Al-4V samples, Appl. Sci. 10 (2020) 1–18.

[25] Z. Liu, G Welsch, Effects of oxygen and heat treatment on the mechanical properties of alpha and beta titanium alloys, Metall. Trans. A 19 (1988) 527–542.

[26] M.J. Bermingham, D.H. StJohn, J. Krynen, S. Tedman-Jones, M.S Dargusch, Promoting the columnar to equiaxed transition and grain refinement of titanium alloys during additive manufacturing, Acta Mater 168 (2019) 261–274.

[27] M. Yan, M.S. Dargusch, T. Ebel, M. Qian, A transmission electron microscopy and three-dimensional atom probe study of the oxygen-induced fine microstructural features in as-sintered Ti-6Al-4V and their impacts on ductility, Acta Mater 68 (2014) 196–206.

[28] R. Hosseini, M. Morakabati, S.M. Abbasi, A. Hajari, Development of a trimodal microstructure with superior combined strength, ductility and creep-rupture properties in a near alpha titanium alloy, Mater. Sci. Eng. A 696 (2017) 155–165.

[29] A.I. Kahveci, G.E. Welsch, Effect of oxygen on the hardness and alpha/beta phase ratio of Ti6A14V alloy, Scr. Metall. 20 (1986) 1287–1290.

[30] M.J. Bermingham, S.D. McDonald, M.S. Dargusch, D.H. Stjohn, Effect of oxygen on the β-grain size of cast titanium, Mater. Sci. Forum 654–656 (2010) 1472–1475.

[31] D.D. Harwig, C. Fountain, W. Ittiwattana, H. Castner, Oxygen equivalent effects on the mechanical properties of titanium welds, Weld. J. 79 (2000) 305-s.

[32] S.D. Luo, et al., High oxygen-content titanium and titanium alloys made from powder, J. Alloys Compd. 836 (2020).

[33] Y. Cui, K. Aoyagi, Y. Koizumi, T. Fujieda, A Chiba, Enhanced oxidation resistance of a titanium–based alloy by the addition of boron and the application of electron beam melting, Addit. Manuf. 31 (2020) 100971.

[34] W.A. Grell, et al., Effect of powder oxidation on the impact toughness of electron beam melting Ti-6Al-4V, Addit. Manuf. 17 (2017) 123–134.

[35] A. Caballero, J. Ding, Y. Bandari, S. Williams, Oxidation of Ti-6Al-4V during wire and arc additive manufacture. *3D print*, Addit. Manuf. 6 (2019) 91–98.

[36] R.R. Boyer, An overview on the use of titanium in the aerospace industry, Mater. Sci. Eng. A 213 (1996) 103–114.

[37] M. Lopez, et al., Effects of postprocess hot isostatic pressing treatments on the mechanical performance of EBM fabricated TI-6Al-2Sn-4Zr-2Mo, Materials (Basel) 13 (2020).

[38] A. Chamanfar, T. Pasang, A. Ventura, W.Z. Misiolek, Mechanical properties and microstructure of laser welded Ti-6Al-2Sn-4Zr-2Mo (Ti6242) titanium alloy, Mater. Sci. Eng. A 663 (2016) 213–224.

[39] D. Ballat-Durand, S. Bouvier, M. Risbet, W. Pantleon, Through analysis of the microstructure changes during linear friction welding of the near-α titanium alloy Ti-6Al-2Sn-4Zr-2Mo (Ti6242) towards microstructure optimization, Mater. Charact. 151 (2019) 38–52.

[40] C.L.A. Leung, et al., Effect of preheating on the thermal, microstructural and mechanical properties of selective electron beam melted Ti-6Al-4V components, Mater. Des. 174 (2019) 107792.

[41] P.D. Lee, T. North, A.R. Perrin, Methods of experimental confirmation of a computational model of the fluid flow in gas tungsten arc welding, Model. Control Cast. Weld. (1988).

[42] K.C. Mills, B.J. Keene, R.F. Brooks, A Shirali, Marangoni effects in welding, Philos. Trans. R. Soc. A Math. Phys. Eng. Sci. 356 (1998) 911–925.

[43] T.N. Le, Y.L Lo, Effects of sulfur concentration and Marangoni convection on melt-pool formation in transition mode of selective laser melting process, Mater. Des. 179 (2019) 107866.

[44] Y. Wang, H.L Tsai, Effects of surface active elements on weld pool fluid flow and weld penetration in gas metal arc welding, Metall. Mater. Trans. B Process Metall. Mater. Process. Sci. 32 (2001) 501–515.

[45] L. Aucott, et al., Revealing internal flow behaviour in arc welding and additive manufacturing of metals, Nat. Commun. 9 (2018) 1–7.

[46] C.R. Heiple, J.R. Roper, Mechanism for minor element effect on GTA fusion zone geometry, Weld. J. (1982) 61.

[47] C. Li, Y. Shi, Y. Gu, F Yang, Effect of oxide on surface tension of molten metal, RSC Adv. 7 (2017) 53941–53950.

[48] Y. Chen, et al., Synchrotron X-ray imaging of directed energy deposition additive manufacturing of titanium alloy Ti-6242, Addit. Manuf. 41 (2021) 101969.

[49] H. Kügler, Effects of short-term laser beam heating on the absorptivity of steel sheets, J. Manuf. Mater. Process. 3 (2019).

[50] A.M. Rubenchik, et al., Temperature-dependent 780-nm laser absorption by engineering grade aluminum, titanium, and steel alloy surfaces, Opt. Eng. 53 (2014) 122506.

[51] Khorasani, A.M., Gibson, I. & Ghaderi, A.R. Rheological characterization of process parameters influence on surface quality of Ti-6Al-4V parts manufactured by selective laser melting. V, 3761–3775 (2018).

[52] V.V. Popov, A. Katz-Demyanetz, A. Garkun, M. Bamberger, The effect of powder recycling on the mechanical properties and microstructure of electron beam melted Ti-6Al-4 V specimens, Addit. Manuf. 22 (2018) 834–843.

[53] H.P. Tang, et al., Effect of powder reuse times on additive manufacturing of Ti-6Al-4V by selective electron beam melting, Jom 67 (2015) 555–563.

[54] G. Soundarapandiyan, et al., The effects of powder reuse on the mechanical response of electron beam additively manufactured Ti6Al4V parts, Addit. Manuf. 46 (2021).

[55] C.L.A. Leung, et al., The effect of powder oxidation on defect formation in laser additive manufacturing, Acta Mater 166 (2019) 294–305.

[56] P.A. Kobryn, S.L. Semiatin, Microstructure and texture evolution during solidification processing of Ti-6A1-4V, J. Mater. Process. Technol. 135 (2003) 330–339.

[57] T. Sugahara, et al., The effect of Widmanstätten and equiaxed microstructures of Ti-6Al-4V on the oxidation rate and creep behavior, Mater. Sci. Forum 636–637 (2010) 657–662.

[58] I. Bantounas, T.C. Lindley, D. Rugg, D. Dye, Effect of microtexture on fatigue cracking in Ti-6Al-4V, Acta Mater 55 (2007) 5655–5665.

[59] W. Xu, E.W. Lui, A. Pateras, M. Qian, M. Brandt, In situ tailoring microstructure in additively manufactured Ti-6Al-4V for superior mechanical performance, Acta Mater 125 (2017) 390–400.

[60] S. Liu, Y.C. Shin, Additive manufacturing of Ti6Al4V alloy : a review, Mater. Des. 164 (2019) 107552.

[61] Z. Zou, M. Simonelli, J. Katrib, G. Dimitrakis, R Hague, Refinement of the grain structure of additive manufactured titanium alloys via epitaxial recrystallization enabled by rapid heat treatment, Scr. Mater. 180 (2020) 66–70.

[62] Y. Zhu, X. Tian, J. Li, H. Wang, Microstructure evolution and layer bands of laser melting deposition Ti-6.5Al-3.5Mo-1.5Zr-0.3Si titanium alloy, J. Alloys Compd. 616 (2014) 468–474.

[63] K. Kapoor, et al., Materials Characterization Strain rate sensitivity, microstructure variations, and stress-assisted $\beta \rightarrow \alpha''$ phase transformation investigation on the mechanical behavior of dual-phase titanium alloys, Mater. Charact. 166 (2020) 110410.

[64] M.J. Donachie Jr., Understanding the metallurgy of titanium crystal structure and alloy types, Titan. A Tech. Guid. (2000) 13–24, doi:10.1361/tatg2000p013.

[65] A. Shaikh, et al., Effect of temperature and cooling rates on the $\alpha+\beta$ morphology of Ti-6Al-4V alloy, Procedia Struct. Integr. 14 (2019) 782–789.

[66] C. Tan, Y. Fan, Q. Sun, G Zhang, Improvement of the crack propagation resistance in an $\alpha + \beta$ titanium alloy with a trimodal microstructure, Metals (Basel) 10 (2020) 1–11.

[67] Termini, E. et al. Alexandra Thesis. 21, 1–9 (2020).

[68] M. Donachie Jr., understanding the metallurgy of titanium crystal structure and alloy types, Titanium: Techn. Guide (2000) 13–24, doi:10.1361/tatg2000p013.

[69] Lu, S., Fujii, H., Sugiyama, H., Tanaka, M. & Nogi, K. Weld penetration and Marangoni convection with oxide fluxes in GTA welding. 43, 2926–2931 (2002).

[70] Gonza, M.L., Society, M. & Tio, B. XPS analysis of Ti6Al4V oxidation under UHV conditions. 45, 6285–6290 (2014).

[71] A. Kaur, P. Chahal, T Hogan, Selective fabrication of SiC/Si diodes by excimer laser under ambient conditions, IEEE Electron Device Lett 37 (2016) 142–145.

[72] J. Dai, J. Zhu, C. Chen, F. Weng, High temperature oxidation behaviour and research status of modifications on improving high temperature oxidation resistance of titanium alloys and titanium aluminides: a review, J. Alloys Compd. 685 (2016) 784–798.

[73] A. Knaislov, P. Nov, M. Cabibbo, L Jaworska, Development of TiAl – Si alloys — a review, Materials (Basel) 14 (2021) 1–22.

[74] D. Vojtěch, B. Bártová, T. Kubatík, High temperature oxidation of titanium-silicon alloys, Mater. Sci. Eng. A 361 (2003) 50–57.